

# Experimental and Computational Assessment of a Ducted-Fan Rotor Flow Model

Ali Akturk\* and Cengiz Camci†

Pennsylvania State University, University Park, Pennsylvania 16802

DOI: 10.2514/1.C031562

Ducted-fan-based vertical and/or short takeoff and landing uninhabited aerial vehicles are frequently encountered in aeronautical applications. In edgewise flight, the performance of these vehicles is, in general, poor because of the increasingly distorted inlet flow as the flight speed is increased. The present experimental study uses a planar particle image velocimeter system to investigate the near duct aerodynamic performance in hover and edgewise flight conditions. High-resolution particle image velocimetry measurements provide reliable and high-resolution aerodynamic data forming a validation basis for further analytical and computational design studies. A radial equilibrium-based fan aerodynamic model is also integrated into a three-dimensional Reynold-averaged-Navier–Stokes-based computational system. Particle image velocimetry measurements and computational predictions of the mean flow near the fan inlet plane are in very good agreement at hover conditions. The aerodynamic modifications due to fan inlet flow distortion in an edgewise flight regime are clearly displayed in particle image velocimetry results. A comparison of the current particle image velocimetry measurements and the accelerated Reynold-averaged-Navier–Stokes predictions supported by the simple radial equilibrium-based rotor model indicates that the current rotor model can be highly effective and time efficient in the design cycle of future vertical and/or short takeoff and landing uninhabited aerial vehicle systems based on ducted fans.

## Nomenclature

$c_x$	=	axial velocity
$c_\theta$	=	tangential (swirl) velocity component
$c_1, c_2$	=	rotor inlet and exit absolute velocity
$p$	=	static pressure
$P_0$	=	total pressure
$r$	=	radial distance measured from origin
$w_1, w_2$	=	rotor inlet and exit relative velocity
$\beta_1, \beta_2$	=	blade inlet and exit angle measured from axial direction
$\rho$	=	density
$\Omega$	=	rotational speed, rad/s

## I. Introduction

**D**UCTED fans that are widely used propulsion systems in vertical and/or short takeoff and landing (V/STOL) uninhabited aerial vehicles (UAVs) offer a higher static thrust/power ratio for a given diameter than open propellers. This is the result of diffusion of the propeller jet stream. They also provide impact protection for the rotating blades and improve personnel safety due to the enclosed fan structure as well as the lower noise level in the plane of the rotating fan blade.

The viscous flow characteristics of the ducted fan are complex. These vehicles need to be capable of flight in a broad range of atmospheric conditions, including the complex turbulent flowfields around buildings and trees. When a V/STOL ducted fan is in

edgewise flight, because of the relative inlet flow dominantly parallel to its rotor inlet plane, flow separation at the leading-edge duct lip is encountered. The inlet flow separation leads to problems within the duct and may well result in a high pitchup moment as the edgewise flight speed is increased. Excessive vibration in such systems is also reported. Therefore, measuring and predicting the three-dimensional (3-D) mean flow characteristics of ducted fans is crucial to understand the problems related to reliable and controllable edgewise flights. Numerous studies have been undertaken in order to quantify the flowfield properties in and around ducted fans. The operation of an axial flow fan with strong inlet flow distortion severely affects the performance of the rotor especially near the tip region of the blades.

Experimental investigation has been the major approach to study the mean flow characteristics of the ducted fan. Abrego and Bulaga [1] performed wind-tunnel tests to determine the performance characteristics of ducted fans for axial and edgewise flight conditions. Their study resulted in showing the important effect of exit vane flap deflection and flap chord length on side force generation. Martin and Tung [2] tested a model ducted-fan V/STOL UAV with a 10-in.-diam fan rotor. They measured aerodynamic loads on the vehicle for different angles of attack in hover and different crosswind velocities. They also included hot-wire velocity surveys at inner and outer surfaces of the duct and across the downstream wake, emphasizing the effect of tip gap on the thrust force produced. In addition, their study showed the effect of leading-edge radius of the duct on the stall performance and stability of the vehicle. Fleming et al. [3] conducted wind-tunnel experiments and computational studies around a 12-in.-diam ducted fan. They concentrated on the performance of ducted-fan V/STOL vehicles in a crosswind.

Moreover, the ducted-fan design and performance analysis were widely performed by using computational flow modeling. Lind et al. [4] carried out a computational study using a panel method. They compared their results to the experimental results from Martin and Tung [2]. Graf et al. [5] improved ducted-fan edgewise flight performance with a recently designed leading-edge geometry, which was a significant factor in offsetting the effects of the adverse aerodynamic characteristics. He and Xin [6] developed their ducted-fan models based on a nonuniform and unsteady ring-vortex formulation for the duct and blade element model for the fan. Numerical studies in axial flight and crosswind were conducted and validated against measured data. Chang and Rajagopalan [7]

Presented as Paper 2009-0332 at the 47th AIAA Aerospace Sciences Meeting, Orlando, FL, 5–8 January 2009; received 22 June 2011; revision received 14 October 2011; accepted for publication 21 November 2011. Copyright © 2011 by Cengiz Camci and Ali Akturk. Published by the American Institute of Aeronautics and Astronautics, Inc., with permission. Copies of this paper may be made for personal or internal use, on condition that the copier pay the \$10.00 per-copy fee to the Copyright Clearance Center, Inc., 222 Rosewood Drive, Danvers, MA 01923; include the code 0021-8669/12 and \$10.00 in correspondence with the CCC.

\*Postdoctoral Research Fellow, Turbomachinery Aero-Heat Transfer Laboratory, Vertical Lift Research Center of Excellence, Department of Aerospace Engineering.

†Professor of Aerospace Engineering, Turbomachinery Aero-Heat Transfer Laboratory, Vertical Lift Research Center of Excellence, Department of Aerospace Engineering.

developed an accurate grid generation methodology known as the curve adaptive option to model several industrial ducted fans. An axisymmetric, incompressible Navier–Stokes solver was applied to calculate the flowfield of a ducted fan. Their computational results agreed well with available wind-tunnel test data. Ahn and Lee [8] applied a computational method to their ducted-fan system to identify the design parameters that affect its performance. Their ducted-fan system was designed by using a stream-surface-based axisymmetric analysis that provided the physical characteristics and design parameters of the system. Ko et al. [9] developed a computer code, aiming the preliminary design of a ducted-fan system. This code was validated using data from many wind-tunnel and flight tests. Furthermore, it was extensively used in the design of commercial ducted fans. Recently, Zhao and Bil [10] proposed a computational fluid dynamics (CFD) simulation to design and analyze an aerodynamic model of a ducted-fan UAV in the preliminary design phase with different speeds and angles of attack.

The current study uses a simultaneous experimental and computational approach around a ducted fan that has a 5 in. diameter. By these analyses, a complicated flowfield around the ducted fan in hover and edgewise flight conditions is investigated. Flow features such as inlet lip separation, distortion of inlet flow features before and after the axial fan rotor, influence of rotor tip speed, influence of edgewise flight velocity, and the interaction of the crosswind with fan exit jet are investigated through experiments and computations. For high-resolution mean flow experiments, a particle image velocimeter (PIV) is used. Axial and radial velocity components at the inlet/exit region of the ducted fan are measured in hover and edgewise flight. By measuring axial and radial velocity components, the effect of leading-edge duct lip separation on the flowfield into the fan rotor is quantified and analyzed.

For the current computational investigations, 3-D incompressible Reynolds-averaged Navier–Stokes (RANS) equations are solved using a general-purpose fluid mechanics solver, ANSYS FLUENT. To accelerate the viscous flow computations, a custom-developed rotor disk flow model based on the radial equilibrium equation, the energy equation, and the conservation of angular momentum principle is integrated into the viscous flow solver. The specific radial equilibrium-theory-based fan-model implemented in this study uses a prescribed static pressure rise across the rotor disk for a time efficient simulation of the fan rotor in the RANS computational environment. The paper describes a method to compute the static pressure rise at each radial position of the rotor blade in the function of the rotor exit absolute velocity. A comparison of the current PIV measurements and the RANS predictions supported by the simple radial equilibrium-based rotor model indicates that current computational approaches can be highly effective and time efficient in the design of future V/STOL UAV systems based on ducted fans. Time-efficient and reasonably accurate rotor flow models developed in this study are essential in the highly iterative design and optimization cycles of ducted-fan-based V/STOL UAV systems.

## II. Experimental Setup

A test rig is designed and manufactured to investigate the local flow features in and around a 5-in.-diam. ducted fan using a planar PIV system. The ducted fan under investigation has a high-speed five-bladed rotor operating in a low-Reynolds-number environment because of short blade heights inherent to the current ducted fan. The high-speed rotor exit flow is challenging because of inlet lip separation in edgewise flow, tip leakage related complications, hub separation, and leading-edge stall unique to this five-bladed rotor. The experimental setup also has provisions for seeding the fan flowfield with a fluidized bed-driven smoke-generator system using fog fluid that is a mixture of triethylene glycol, propylene glycol, butylene glycol, and deionized water. Figure 1 shows a sketch of the current experimental setup.

### A. Ducted-Fan Model

The five-bladed ducted-fan rotor is driven by a high-efficiency brushless dc electric motor that is speed-controlled by an electronic speed control system. The high-efficiency electric motor driving the fan can deliver 1.5 kW of power (2.14 hp) and spin at 1050 rpm per volt supplied to the motor. The ducted fan provides a disk loading range from 345 to 976 Pa in a corresponding rotor speed range from 9000 to 15,000 rpm. The rotor tip speed-based Reynolds number at 15,000 rpm is approximately 168,000. The Reynolds numbers at midspan and rotor hub are about 115,000 and 70,000, respectively, at 15,000 rpm. The phase-locked PIV measurements are triggered by using an optical once-per-revolution device located near the hub of the rotor exit. An infrared beam is reflected from a highly reflective (1-mm-wide metallic film) attached to the rotor hub. This once-per-revolution pulse provides a phase-locked triggering of the PIV data collection system. The position of the rotor can be adjusted accurately in relation to the position of the laser light sheet that contains the rectangular PIV measurement domain. The PIV domain can be located at the upstream and downstream of the rotor as shown in Fig. 1. Figure 2 shows the five-bladed ducted fan that is used in the present PIV experiments. The geometric specifications of the rotor system are presented in Tables 1 and 2.

The specific ducted-fan unit used in this study is designed for small-scale uninhabited flying vehicles. This unit is manufactured from carbon composite material and has five rotor blades and six outlet guide vanes at the exit of the fan in order to remove some of the swirl and torque existing at the exit of the rotor. A tail cone is used to cover the motor surface and hide the electrical wiring, as shown in Fig. 2.

### B. Crosswind Blower

Figure 1 shows a sketch of the crosswind blower that can generate a uniform mean flow just upstream of the ducted-fan unit. The ducted-fan unit is at 90 deg angle of attack with respect to the

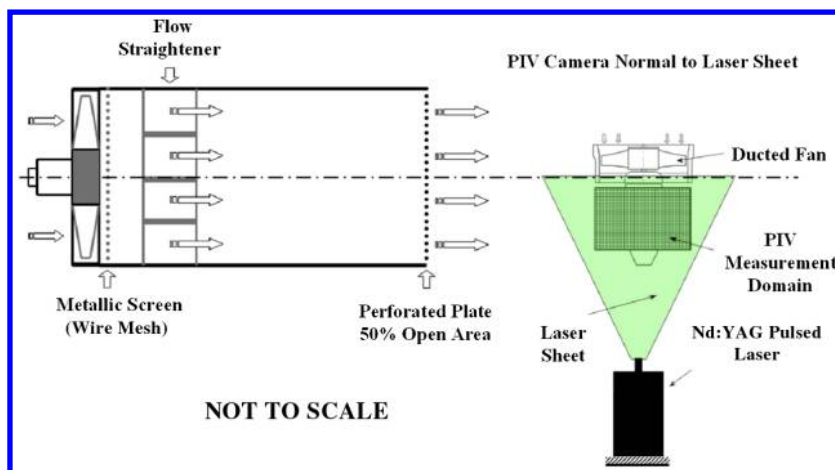


Fig. 1 Crosswind blower, ducted fan, and PIV system orientation.

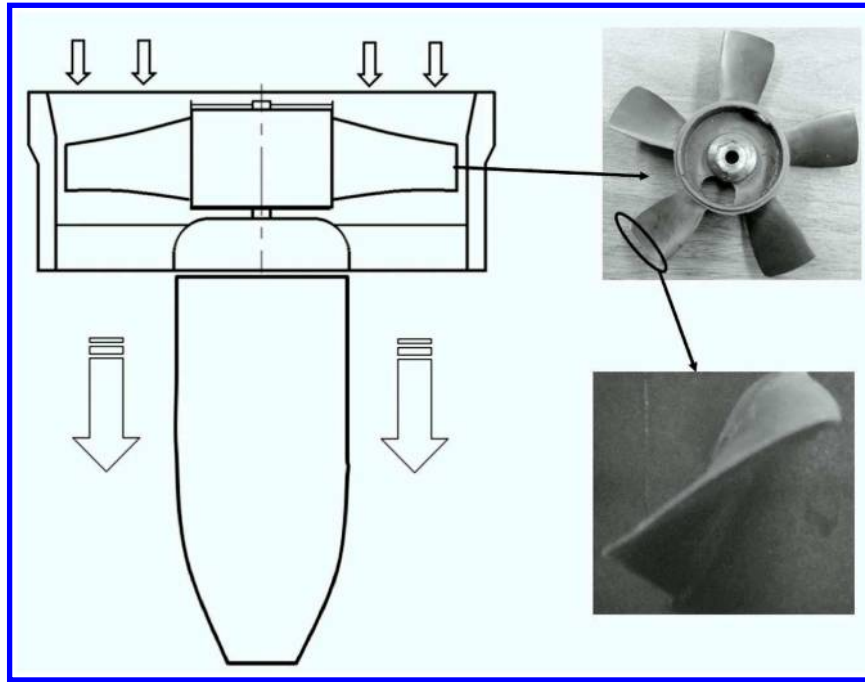


Fig. 2 Five-in.-diam five-bladed ducted fan.

airstream generated by the cross-stream blower, as shown in Fig. 1. The axial flow fan driving the crosswind blower is capable of generating  $5.58 \text{ m}^3/\text{s}$  (10,594 cfm). There is a wire mesh screen just downstream of the axial flow fan for turbulent flow management purposes. The flow passes through a 10-in.-wide flow straightener section. Finally, there is a perforated plate (50% open area) at the exit of the crosswind blower. The grill, flow straightener, and perforated plate at the exit provide a uniform mean flow at the exit of the system. The uniformity of the blower exit mean flow (6 m/s) is determined by a hot-wire anemometer. The measured turbulence intensity of the uniform flow is about 0.9% based on the rms fluctuation velocity fluctuations normalized by the mean flow magnitude. An ac inverter connected to the three-phase ac motor of the axial fan unit can adjust the rotor revolutions per minute and mean flow velocity magnitude coming out of the cross-stream blower.

### III. Experimental Method

The planar PIV technique measures instantaneous velocity components of a flowfield over a determined area in a planar light sheet generated by a pulsed Nd:YAG laser. The general attributes of the specific planar PIV method are explained in detail in [11–16]. Small particles existing in a fog generated by a fluidized bed system are introduced into the fluid flow, and the region of interest is illuminated by a light sheet provided by short and multiple Nd:YAG laser pulses lasting as short as a few nanoseconds. Nd:YAG laser emits visible green light at 532 nm after frequency doubling of the infrared emission at 1064 nm originally produced at the laser cavity. The subsequent step is the recording of the displacement of particles

via one or two charge-coupled device (CCD) cameras, depending on the specific PIV technique used. The four basic steps of a typical planar PIV measurement can be summarized as follows:

- 1) Flow is seeded.
- 2) The flow region of interest is illuminated.
- 3) Scattering light from the particles forming the speckle images is recorded by a camera.
- 4) Recordings are analyzed by means of a correlation-based software system.

In this current study, the inlet and exit mean flow performance of the 5-in.-diam ducted fan was quantified by using the PIV technique. Axial and radial components of velocity profiles were measured near the inlet and exit planes of the ducted fan. Two separate measurement domains of  $156 \times 96 \text{ mm}$  are used in inlet and exit flows. Figure 1 illustrates the PIV setup in which the fan exit field is measured by keeping the PIV light sheet unchanged. For the measurement of inlet flow velocities, the ducted fan is flipped vertically and rotated 180 deg in a counterclockwise direction. The PIV measurement domains are illuminated by a double-cavity frequency-doubled pulsating Nd:YAG laser that has a final emitted radiation wavelength of 532 nm (green) and 120 mJ maximum pulse energy level. Pairs of images from measurement domains are captured by an 80C60 HiSense PIV/planar laser-induced fluorescence PLIF camera. The CCD camera is positioned normal to the laser sheet.

In planar PIV measurements, two components of the velocity vector are measured in the plane illuminated by a laser sheet. The current study focuses on measuring the axial and radial components of the local velocity vectors based on the image maps obtained by the CCD camera. The approximate size of the seeding particle is in a range between  $0.25\text{--}60 \text{ }\mu\text{m}$ . The image pairs of PIV domains are recorded. The image maps are divided into  $32 \times 32$  pixel interrogation areas, and 25% overlapping is used. The FlowMap software provided by DANTEC [15] is used for capturing PIV images and correlation analysis. All 700 image pairs are adaptive correlated, moving average validated, and then ensemble averaged to obtain true

Table 1 Geometric specifications of the current ducted-fan rotor system

Parameter	Value
Rotor hub diameter	52 mm
Rotor tip diameter	120 mm
Blade height $h$	34 mm
Tip clearance $t/h$	5.8%
Maximum blade thickness at rotor tip	1.5 mm
Tail cone diameter	52 mm
Tail cone length	105 mm
Rotor tip $Re$ at 9000 rpm	100,000
Rotor tip $Re$ at 15,000 rpm	168,000

Table 2 Rotor blade section properties

	Hub	Midspan	Tip
Blade inlet angle $\beta_1$ , deg	60	40	30
Blade exit angle $\beta_2$ , deg	30	45	60
Blade chord, mm	32	30	28



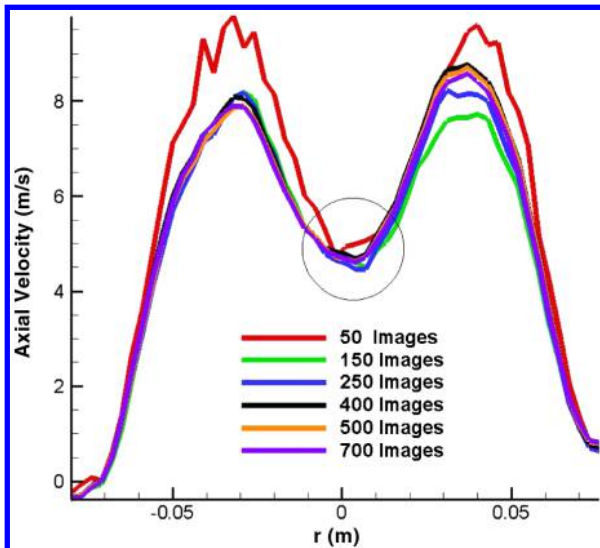


Fig. 3 Influence of ensemble averaging image sample size on the axial velocity component.

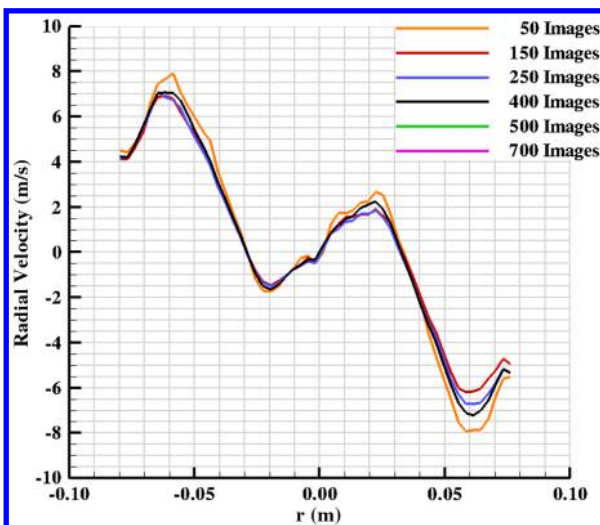


Fig. 4 Influence of ensemble averaging image sample size on the radial velocity component.

mean flow. The ensemble size is of critical importance in achieving statistically stable mean velocity distributions in any PIV data reduction process. Figures 3 and 4 present the influence of the ensemble-averaging sample size on the spanwise distribution of the most significant velocity component that is the axial component. Both figures indicate that an ensemble size of 400 is sufficient in achieving a statistically stable average in the current set of experiments.

## IV. Computational Method

### A. Radial Equilibrium-Based Analysis of Ducted Fan in Hover and Edgewise Flight

A computational simulation of the mean flowfield around the ducted fan was performed by using the general-purpose fluid mechanics solver ANSYS FLUENT. The specific computational system solves the 3-D RANS equations using a finite volume method. The transport equations describing the flowfield are solved in the domain that is presently discretized by using an unstructured computational mesh. A momentum equation and turbulence model equations are discretized using a first-order upwind scheme, while the SIMPLE (semi-implicit method for pressure linked equations) algorithm was used for pressure–velocity coupling. For the analysis of the flowfield around ducted-fan rotors, there are many computational modeling options in general-purpose fluid dynamics solvers. The most complex and time-consuming computational model is the modeling of unsteady/viscous/turbulent flow in and around the fan rotor by using an exact 3-D model of rotor geometry using a sliding mesh technique. This type of solution including a rotating frame of reference is usually lengthy and requires significant computer resources, especially in the edgewise flight mode when an axisymmetric flow assumption is not applicable. The current RANS computations use a custom-developed simplified rotor model, termed a “radial equilibrium-based actuator disk model,” for the generation of the general flow features of the fan rotor. Although the rotor is modeled using an inviscid actuator disk, the flow areas outside the rotor use a  $k$ - $\epsilon$  turbulence model that was invoked for the current computations. The 3-D RANS-based computational method including the custom developed radial equilibrium-based actuator disk is summarized in Fig. 5.

### B. Boundary Conditions

#### 1. Hover

Figure 6 shows the specific boundary conditions and computational domain implemented in the solver for the hover condition. The

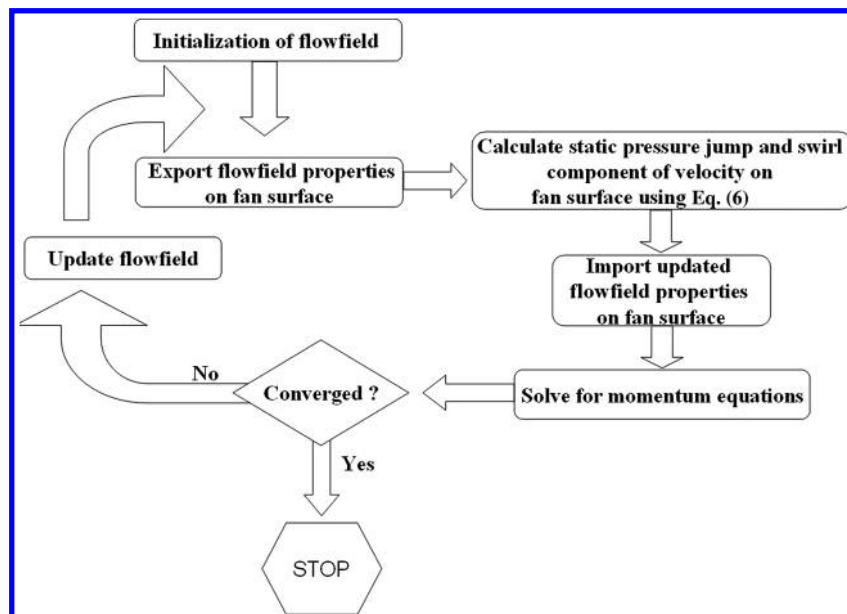


Fig. 5 Flowchart of the 3-D RANS-based computational method including the actuator disk.

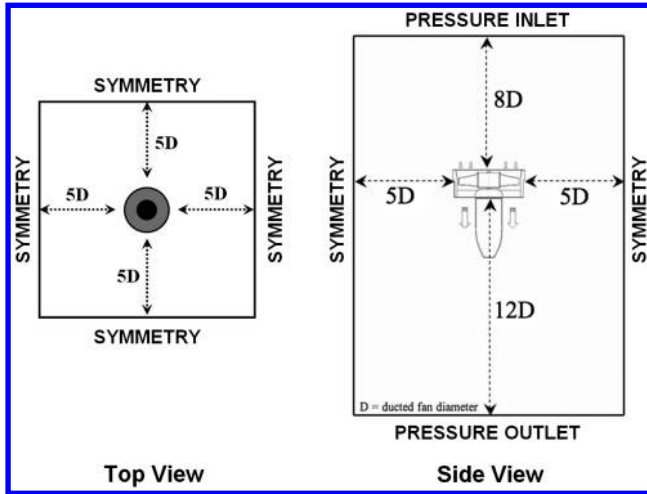


Fig. 6 Boundary conditions for hover.

duct and tail cone surfaces are considered as solid walls with a no-slip condition. On the side surfaces, a symmetry condition is assumed. For the hover condition, a pressure inlet boundary is assumed on the top surface. Atmospheric static pressure is prescribed on the top surface. The pressure inlet boundary is treated as a loss-free transition from stagnation to inlet conditions. The solver calculates the static pressure and velocity at the inlet. Mass flux through the boundary varies depending on interior solution and specified flow direction. A pressure outlet boundary condition is assumed on the bottom surface for the hovering condition. The atmospheric static pressure of the environment into which the flow exhausts is assigned to the pressure outlet boundary. The specific actuator disk model developed from the implementation of the simple radial equilibrium equation in combination with the energy equation and angular momentum conservation equation is described in Sec. IV.C. The implementation of this inviscid rotor representation into a 3-D RANS solver is achieved via a user-defined function (UDF). The actuator disk model effectively simulates the energy addition process to the fluid throughout the rotor. The model contained in the custom-developed UDF is iteratively applied between the inlet and exit surfaces of the rotor plane.

## 2. Edgewise Flight

Figure 7 shows the specific boundary conditions implemented in the 3-D solver for edgewise flight. Like the hover condition, the duct and tail cone surfaces are considered as solid walls with a no-slip condition. The velocity inlet boundary condition is assigned on the windward side of the computational domain. Using this boundary condition, the velocity and turbulent intensity at the windward side are prescribed. For the leeward side of the domain, an outflow condition is assigned. For the top, bottom, and remaining side

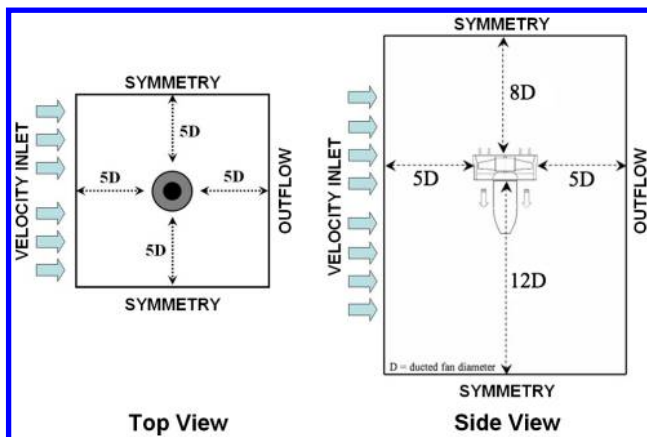


Fig. 7 Boundary conditions for forward flight.

surfaces, a symmetry boundary condition is assigned. A fan-type boundary condition was set using an actuator disk model replacing the ducted-fan rotor similar to hover-related boundary conditions. Details of the custom-developed radial equilibrium-based actuator disk model are explained in Sec. IV.C.

## C. Actuator Disk Model

The complex 3-D rotor flowfield in the rotating frame of reference is replaced by a simplified, inviscid actuator disk model originating from the simultaneous use of the radial equilibrium equation, energy equation, and the conservation of angular momentum principle across the fan rotor. The radial equilibrium equation is the force balance in the radial direction at a given axial position, balancing the pressure forces in the radial direction with the centrifugal force. The viscous effects are ignored in this simplified and easy to implement actuator disk model. Although the blade boundary layers, casing boundary layers, passage secondary vorticity, tip vortices, and hub endwall boundary layer are excluded in this type of energy addition model, the overall characteristics of the rotor flow are approximated in an extremely time-efficient manner. The current study clearly shows that this approach could be instrumental in parametric vehicle design and optimization studies in which computational time efficiency is a major issue to consider.

In this approach, a pressure change term is computed from the first principles at each radial position of the rotor from hub to tip. The magnitude of the static pressure jump term across the rotor is closely related to the amount of stagnation enthalpy change from the rotor inlet to exit. The stagnation enthalpy increase from the rotor inlet to exit is the same as the rate of energy provided to the fluid by the rotor per unit mass flow rate of the duct flow. The conservation of the angular momentum principle and energy equation suggests that the magnitude of this jump is mainly controlled by the tangential (swirl) component  $c_{\theta 2}$  of the flow velocity in the absolute frame of reference at the exit of the rotor and rotor angular velocity.

Figure 8 presents the velocity triangles of the ducted-fan rotor at inlet [Eq. (1)] and exit [Eq. (2)]. The variables  $\beta_1$  and  $\beta_2$  are the blade inlet and exit angles measured from the axial direction. Since the tip Mach number (0.28) of the rotor is not in the compressible flow range, it is reasonable to assume that the internal energy at the rotor inlet  $e_1$  and exit  $e_2$  is approximately the same,  $e_1 = e_2$ . In a ducted-fan rotor, it is realistic to assume that the axial component of the absolute velocity vector is also conserved from inlet to exit  $c_{x2} = c_{x1}$  due to mass conservation considerations. The flow is assumed to be swirl-free and axial at the rotor inlet where  $c_1 = c_{x1}$  and  $c_{\theta 1} = 0$  under design conditions. The relative velocity vector at the exit of the rotor  $w_2$  is smaller than the relative velocity  $w_1$  at the rotor inlet in a typical axial flow fan. While the relative flow  $w_2$  is diffusing in the relative frame of reference, the absolute flow velocity vector  $c_2$  is accelerated at the rotor exit because of added energy to the flow by the rotor.

Equation (1) represents the change of stagnation enthalpy in the ducted-fan rotor system. The right-hand side of this equation is the

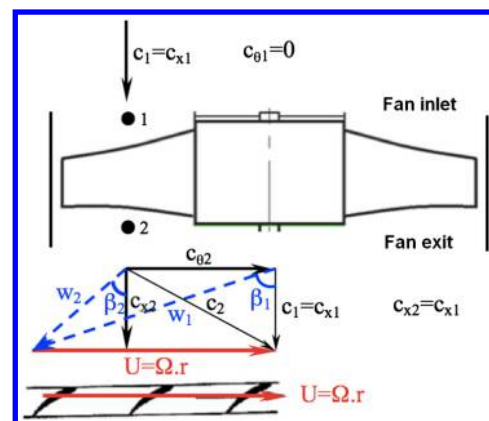


Fig. 8 Velocity triangles at the inlet and exit of the ducted-fan rotor.



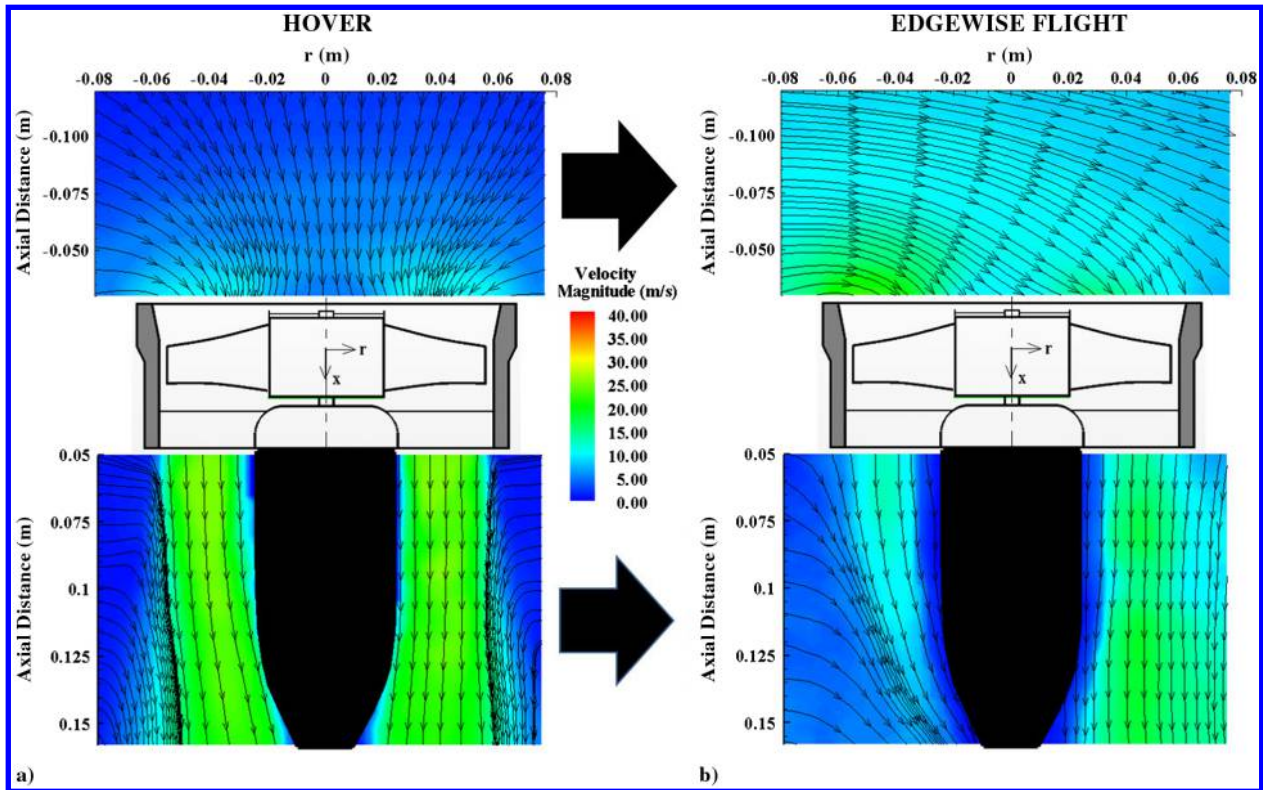


Fig. 9 Streamlines at the inlet and exit of a ducted fan for a) hover and b) edgewise flight (PIV measurements at 9000 rpm).

rate of work per unit mass flow rate of air passing from the rotor. The right-hand side is also the same as the product of the rotor torque and angular speed of the fan rotor:

$$h_{02} - h_{01} = U(c_{\theta 2} - c_{\theta 1}) \quad (1)$$

where

$$U = \Omega r \quad \text{and} \quad c_{\theta 1} = 0$$

$$(h_2 + c_2^2/2) - (h_1 + c_1^2/2) = U c_{\theta 2} \quad (2)$$

$$\left(e_2 + \frac{p_2}{\rho_2} + c_2^2/2\right) - \left(e_1 + \frac{p_1}{\rho_1} + c_1^2/2\right) = U c_{\theta 2} \quad (3)$$

Equation (1) is a simplified form of the energy equation and angular momentum conservation (combined) expressed from rotor

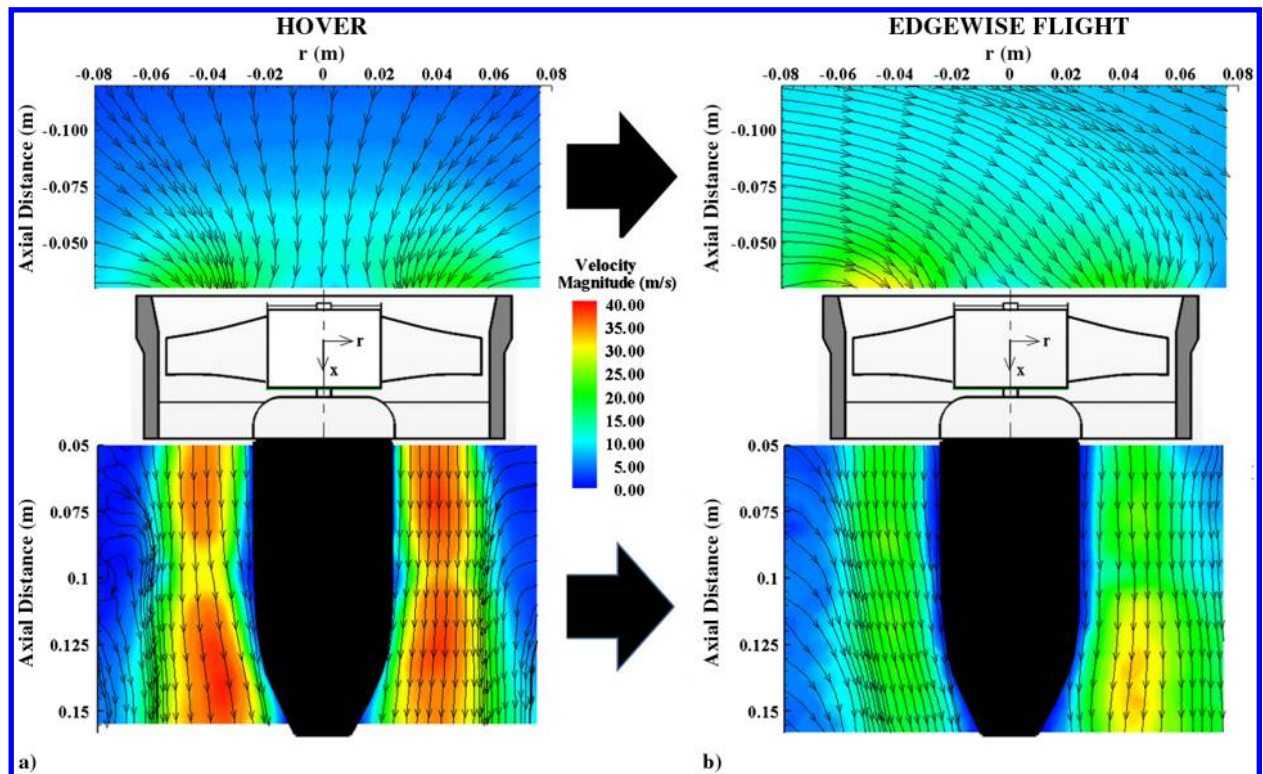


Fig. 10 Streamlines at the inlet and exit of a ducted fan for a) hover and b) edgewise flight (PIV measurements at 15,000 rpm).

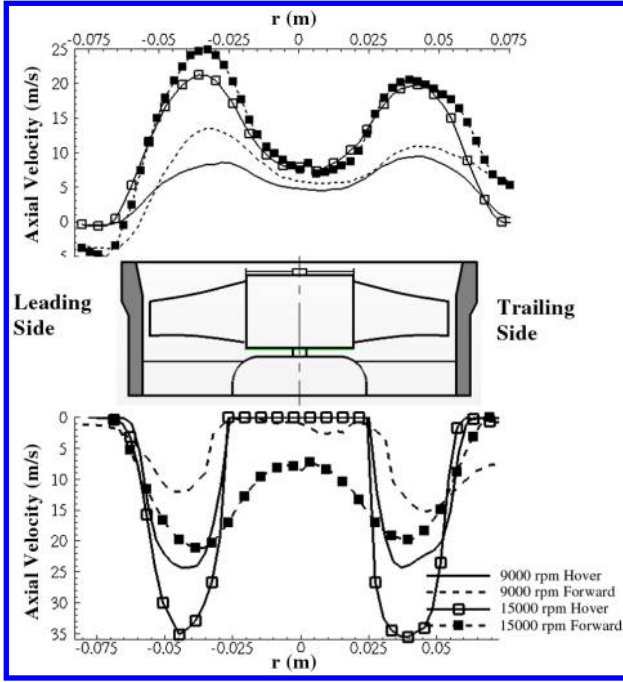


Fig. 11 Axial velocity distribution at the inlet and exit of a ducted fan at 9000 and 15,000 rpm.

inlet to exit of a ducted-fan unit. When  $e_1 = e_2$  is substituted into Eq. (3) because of the incompressibility condition, the Euler equation or pump equation results in Eq. (4). Using Eqs. (4) and (5), an equation for the calculation of the static pressure jump between the rotor inlet and exit can be obtained.

The determination of  $c_{\theta 2}$  is performed by using the velocity triangles as shown in Fig. 8. Since the blade inlet/exit angle distribution for “1” and “2” in the radial direction is known from the existing rotor geometrical properties (shown in Tables 1 and 2),  $w_2$  can be calculated from the assumption that  $c_{x2} = c_{x1} = c_1$ . The absolute rotor exit velocity  $c_2$  is determined by adding  $U = \Omega r$  to  $w_2$  in a vectorial sense:

$$\frac{1}{\rho}(P_{02} - P_{01}) = U c_{\theta 2} \quad (4)$$

Equation (4) could be rearranged as follows:

$$\left(p_2 + \rho \frac{c_2^2}{2}\right) - \left(p_1 + \rho \frac{c_1^2}{2}\right) = \rho U c_{\theta 2} \quad (5)$$

By expressing  $(p_2 - p_1)$  from Eq. (5), a pressure jump statement in the function of radius could be obtained:

$$\Delta p = p_2 - p_1 = \rho[U c_{\theta 2} - \frac{1}{2}(c_2^2 - c_1^2)] \quad (6)$$

Equation (6) allows the enforcing of a prescribed pressure jump  $p$  in the function of density, radial position, rotor angular speed  $\Omega$ , rotor exit swirl velocity  $c_{\theta 2}$ ,  $c_1$ , and  $c_2$ . The rate of energy per unit mass flow rate added to the flow by the rotor is specified by the product  $U c_{\theta 2}$ , as shown in Eqs. (4) and (5). Equation (6) could be evaluated at each radial position between the rotor hub and tip, resulting in the radial distribution of the static pressure jump required by the general-purpose viscous flow solver for a so-called fan-type boundary condition.  $\Delta p$  can be effectively specified in a UDF in the general-purpose solver. The fan-type boundary condition is an effective and time-efficient method of implementing a rotor flowfield via a radial equilibrium-based actuator disk model in a 3-D viscous flow computation.

## V. Experimental Results in Hover and Edgewise Flight Conditions

Experiments were performed at two different rotational speeds at 9000 and 15,000 rpm. The overall performance of the ducted fan was measured and analyzed in hover and edgewise flight conditions. The edgewise flight condition is simulated in laboratory experiments with a crosswind of 6 m/s velocity produced by the crosswind blower, as shown in Fig. 1. The ratios of edgewise flight velocity and axial velocity at midspan is calculated as 0.46 and 0.27 for 9000 and 15,000 rpm, respectively.

Figures 9a and 10a show streamlines obtained from PIV measurements at different rotational speeds (9000 and 15,000 rpm) in hovering. The figures are contour plotted and colored with the magnitude of measured velocity. As expected, the magnitude of velocity is increasing at both inlet and exit regions by increasing the rotational speed of the fan rotor. The streamline structure and the local magnitude of the velocity vector show a reasonable axisymmetry in hover mode, as shown in Figs. 9a and 10a. The exit jet from

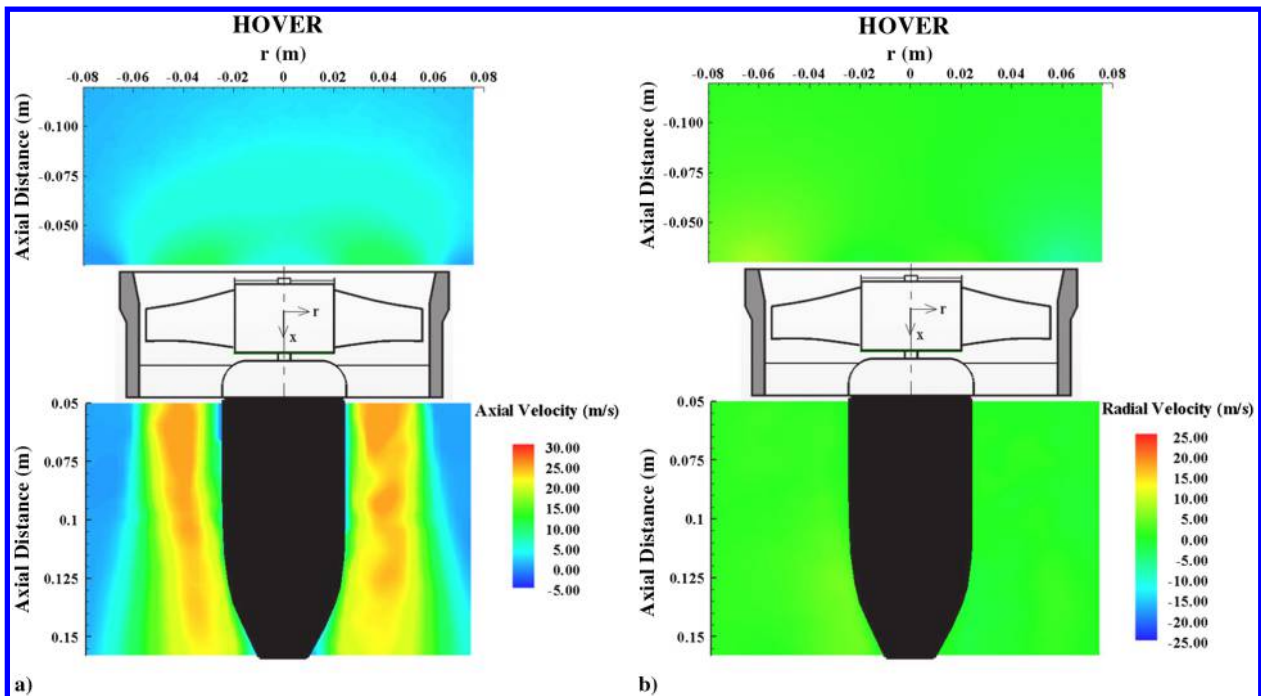


Fig. 12 Velocity components at the hover condition (PIV measurements at 9000 rpm): a) axial and b) radial.



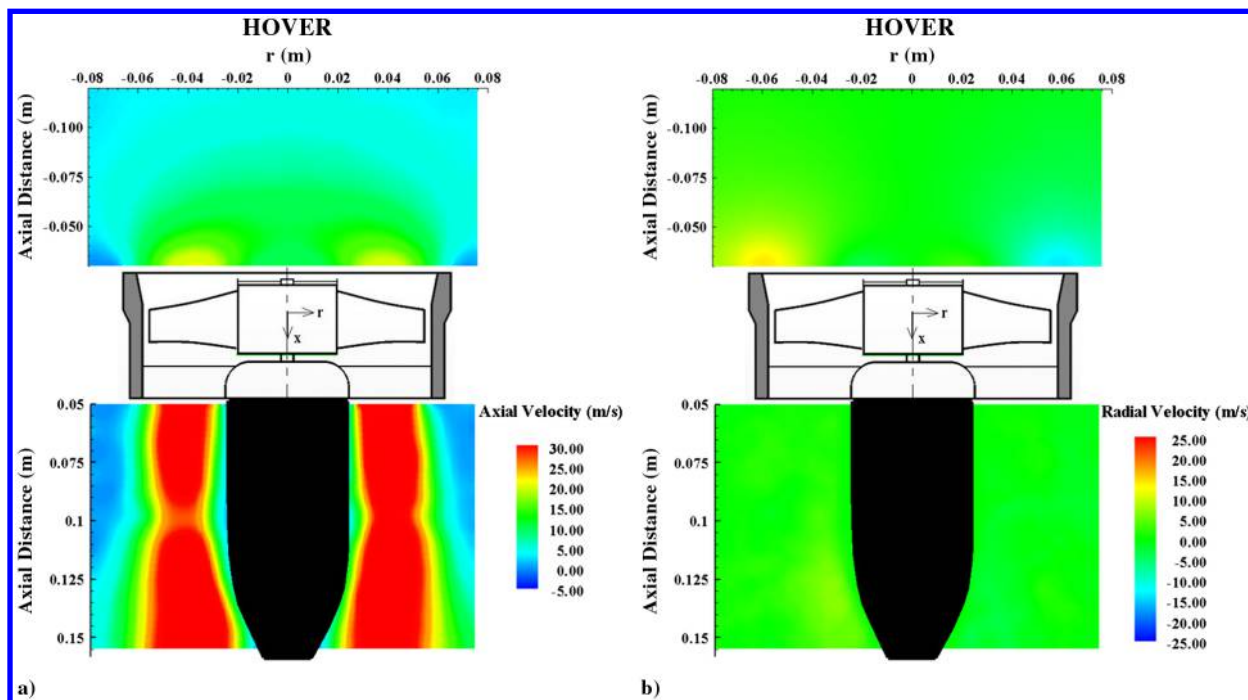


Fig. 13 Velocity components at the hover condition (PIV measurements at 15,000 rpm): a) axial and b) radial.

the fan unit shows a visible flow entrainment from the still-air region into the exit jet at both rotational speeds. In addition to the flow entrainment, the exit jet region at 15,000 rpm exhibits a slight momentum deficit near  $x = 0.1$  m. This momentum deficit could be explained with the existence of the wakes of the six-bladed exit guide vanes in the fan unit. The final form of this distribution is also controlled by the unique rotor position defined by the current phase-locked measurement approach.

Figure 9b illustrates the change of inlet/exit flowfield caused by the edgewise flight effect at 9000 rpm. With the influence of the crosswind at 6 m/s, the distribution of the velocity magnitude at the inlet is distorted due to the separation from the leading-side duct lip. Because of the separation region, the breathing area of the fan rotor is reduced. At the leading side of the duct, the maximum

velocity magnitude is shifted toward the hub because of the effect of lip separation.

Figure 11 clearly supports the observation that the leading-side peak in axial velocity at the inlet plane is shifted toward the rotor hub due to inlet lip separation. However, the trailing-side peak in the inlet plane is shifted toward the blade tip. When the peak is shifted toward the rotor tip section, the work addition to fan exit flow is more significant, as shown in Fig. 11. Because of more distorted inflow at the leading side, the exit flow average velocity magnitude is slightly decreased at the leading side. The streamlines near the trailing side at the inlet plane are more normal to the fan inlet plane, indicating a slightly higher mass flow rate on this side than the leading side of the fan. The trailing side of the duct is affected less from the crosswind. Streamlines at the exit flow clearly show the influence of edgewise

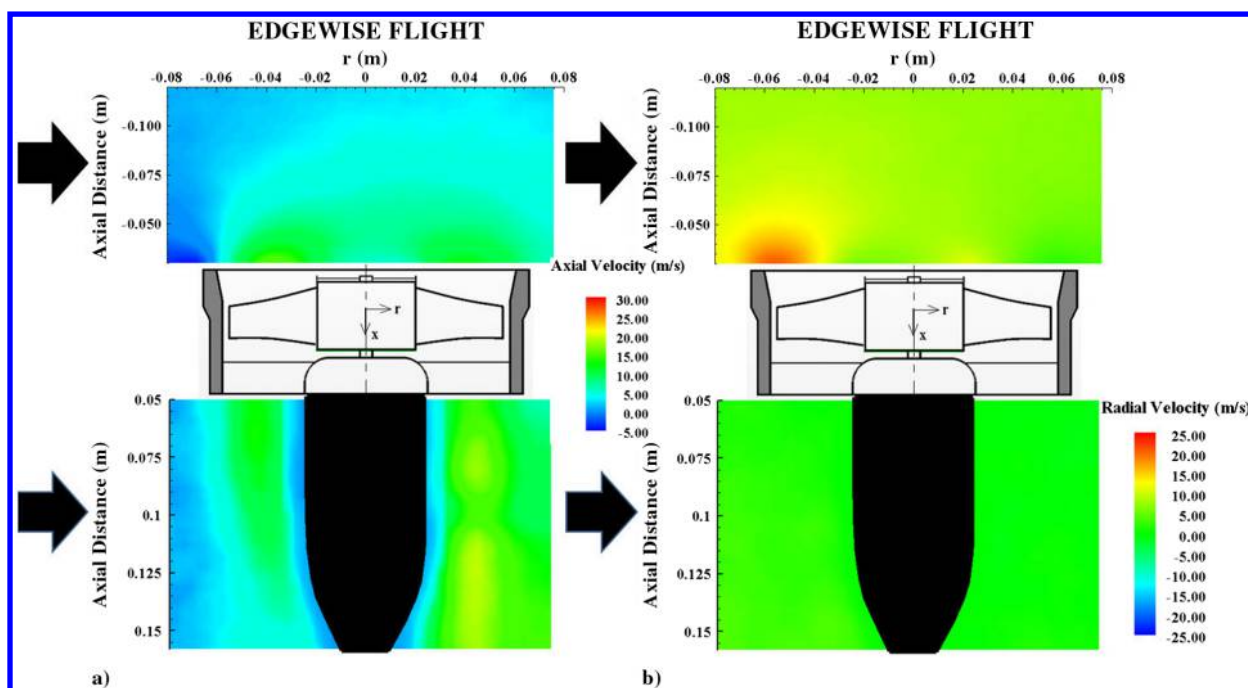


Fig. 14 Velocity components at the edgewise flight condition (PIV measurements at 9000 rpm): a) axial and b) radial.



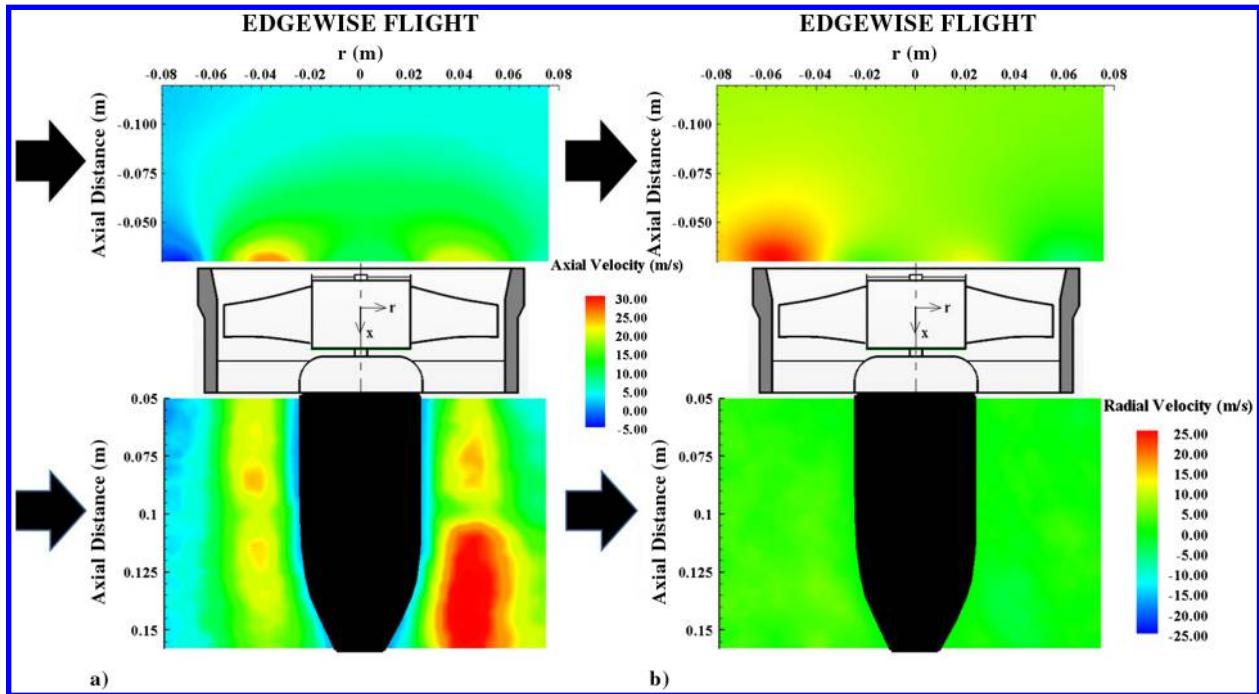


Fig. 15 Velocity components at the edgewise flight condition (PIV measurements at 15,000 rpm): a) axial and b) radial.

flight velocity on the ducted-fan exit flowfield. With the effect of the crosswind, the exit jet is highly deflected and pushed toward the tail cone surface at the leading side of the fan. The trailing-side flow at the fan exit is affected less than the leading side as expected.

The axial velocity plot shown in Fig. 11 is drawn along a horizontal line 3 mm away from the exit and inlet surfaces to demonstrate the effect of crosswind velocity on the axial velocity component. Introduction of the crosswind simulates the edgewise flight conditions. A reduced axial velocity near the leading-edge duct lip is observed in Fig. 11. This reduced axial velocity can be explained by the occurrence of a separation bubble on the leading-side lip inside the duct. Figure 11 also indicates that the axial velocity near the trailing-side lip is relatively enhanced when compared with the hover condition. High velocity near the trailing-side lip is related to the crosswind-induced inlet plane fluid deflected by the separated flow. The flow skipping over the rotating hub also enters the trailing side of the rotor disk at a relatively axial orientation in comparison with the hover conditions.

Figure 10b shows the effects of edgewise flight velocity at 15,000 rpm. An increase in the rotational speed at edgewise flight

effectively energizes the airflow at the inlet. The effect of separation at the leading edge is reduced by the increased rotational speed of the fan. The streamlines near the inlet are more normal to the inlet surface at 15,000 rpm. The streamlines in the exit jet area are much less influenced by the mainstream flow. Figure 10a shows that the mass flow rate passing from the ducted fan at 15,000 rpm is much higher than the case for 9000 rpm. The axial velocity peak in exit plane is almost doubled when the rotational speed is increased to 15,000 rpm.

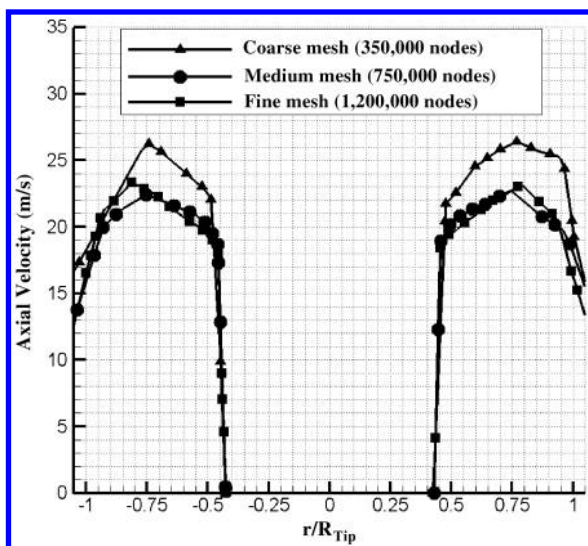


Fig. 16 Grid independence study.

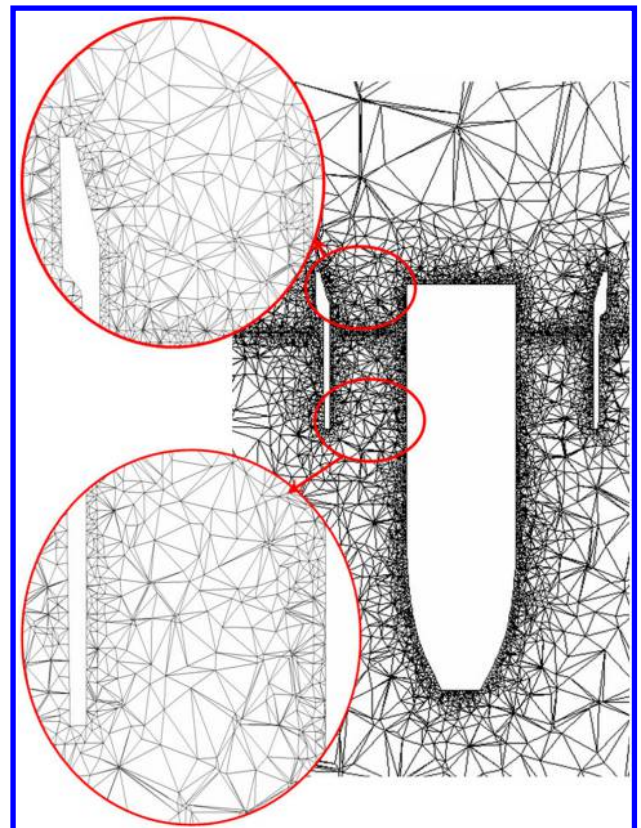


Fig. 17 Medium mesh used in computations.

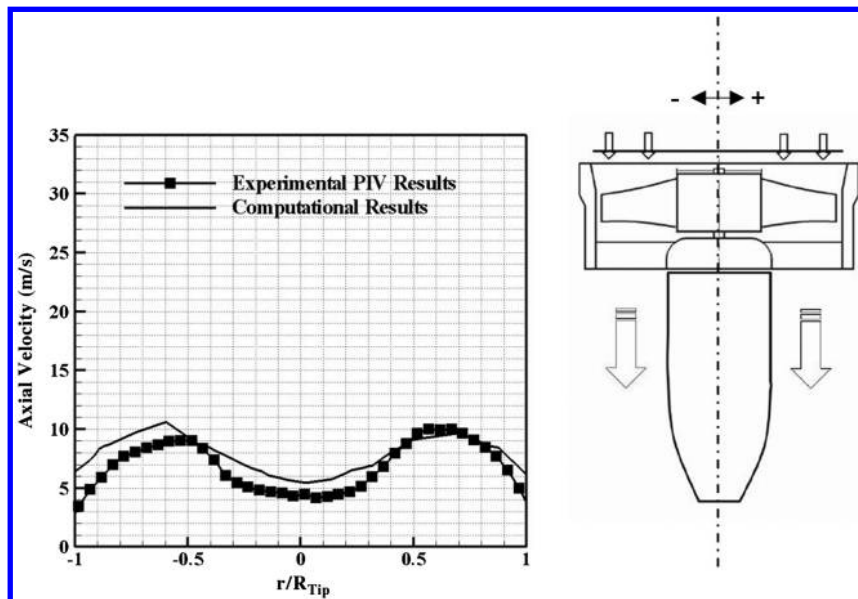


Fig. 18 Comparison of the axial velocity at the fan inlet 3 mm away from the duct surface at a hover condition of 9000 rpm.

Figures 12 and 13 illustrate the axial and radial velocity components at 9000 and 15,000 rpm for the hover condition. An increase in axial velocity by a rotational speed increase results in a significant enhancement of the axial momentum of the system. The radial velocities that are usually in much smaller magnitudes than the axial components show a symmetrical distribution with respect to the axis of rotation. The axial and radial velocity components in the hover condition results in a reasonably uniform distribution of side forces around the duct.

Introducing a crosswind velocity to the field changes the distribution of radial flow velocity around the duct. Figures 14b and 15b indicate an abrupt increase near the leading side of the duct lip. That increase in radial velocity is the result of the strong recirculatory flow near the leading side, as expected. The flow nonuniformities near the leading side of the lip and the strong variations between the leading and the trailing sides of the exit jet result in a strong pitchup moment acting on the ducted fan. It is also observed that, by the increase of rotational speed, the radial velocity is also increasing. But the same amount of increase can also be seen on the radial velocity distribution in the hovering mode. When the rotational speed is increased, the axial momentum of the flow is increased.

## VI. Computational Results

### A. Grid Refinement Study

A grid independence study was performed to show that the computational results are not dependent on the computational mesh and that the resolution of the mesh is adequate to capture the significant flow characteristics. The grid independency is evaluated by comparing the computational solutions from three different mesh sizes comprising a coarse mesh with 350,000 nodes, a medium mesh with 750,000 nodes, and a fine mesh with 1,200,000 nodes. The axial velocity distributions at the exit of the ducted fan are plotted as shown in Fig. 16 for three different grid densities. The profiles suggest that the computational results are grid independent when the 750,000 grid node number is exceeded. Therefore, the medium mesh is used for all predictions in this investigation. Figure 17 shows a view from the mesh used in the current computations.

### B. Model Validation at Hover and Edgewise Flight

#### 1. Hover Condition Results

In this section, the results of 3-D computations using the custom radial equilibrium-based rotor disk model are compared with the PIV

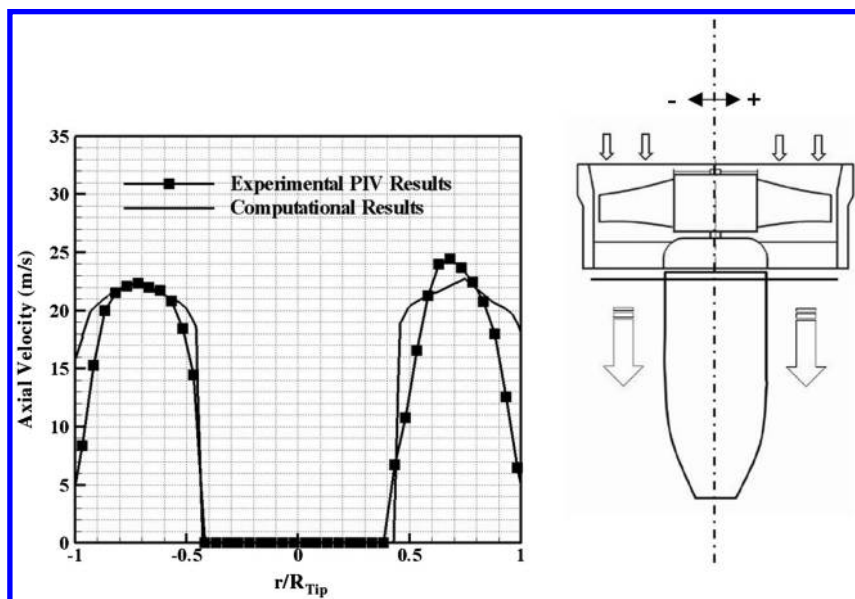


Fig. 19 Comparison of the axial velocity at a fan exit 3 mm away from the duct surface at a hover condition of 9000 rpm.



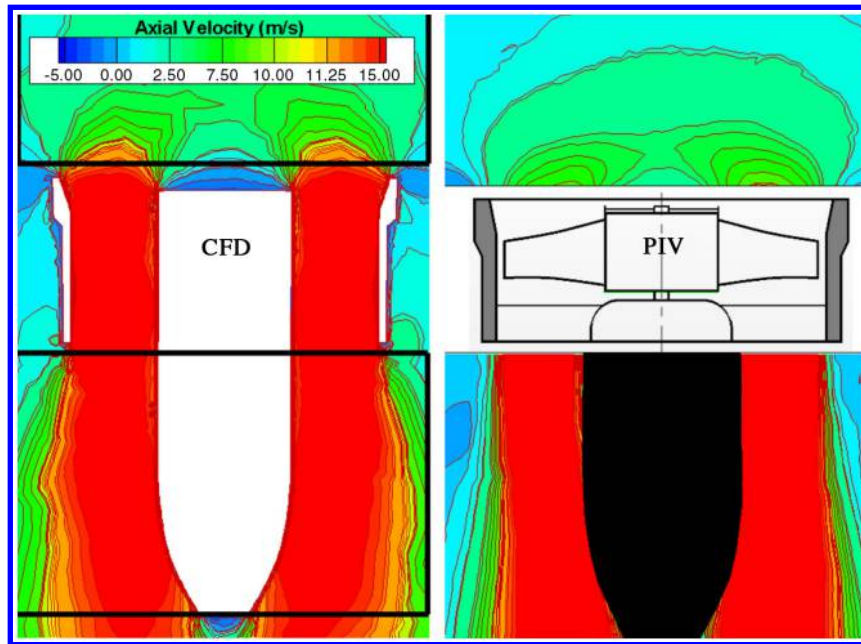


Fig. 20 Comparison of CFD and PIV axial velocity contours at a hover condition of 9000 rpm.

experiments performed for the 5-in.-diam ducted fan. The computed axial velocity component 3 mm away from the duct inlet surface is compared with the results of PIV measurements, as shown in Fig. 18. The computational and experimental results are in good agreement near the leading side of the fan at the inlet plane. The computational predictions near the leading side and the trailing side show an almost symmetrical axial velocity distribution.

The simulation underpredicts the flow as measured by PIV near the trailing side of the duct, as shown in Fig. 18. In a phase-locked PIV approach, measurements are always performed at the same circumferential position of the rotor blade. Since we used a five-bladed fan rotor, the right side of the domain in Fig. 18 contains a rotor blade in the laser sheet. However, the left side of the domain, where  $r \leq 0$ , does not contain a rotor blade in the laser sheet. The slight underprediction is related to the specific phase-locked position of the rotor during the PIV measurements. Because of the blockage effect introduced by the rotor blade in the laser sheet plane, the PIV

measured axial flow velocity magnitude is slightly altered when compared with the computational result.

The comparison of PIV measurements and computed axial velocity components 3 mm away from the duct exit surface are shown in Fig. 19. Since the computational method does not take tip losses, casing boundary layers and secondary flows into account, there is an overprediction of axial velocity near the casing of the ducted fan. It can also be observed that the rotating rotor hub related losses are not predicted well by the current computations.

Figure 20 shows comparison of contour plots obtained from the computational predictions and PIV measurements. Computational results are slightly overpredicting the measured axial velocity at the inlet of the ducted fan. In addition, predictions near the hub are lower than the measurements because the rotating hub is not simulated in the computations. The hub separation usually exists in a small diameter of ducted-fan rotors where the near-hub region exhibits a very complex relatively low-Reynolds-number flow with

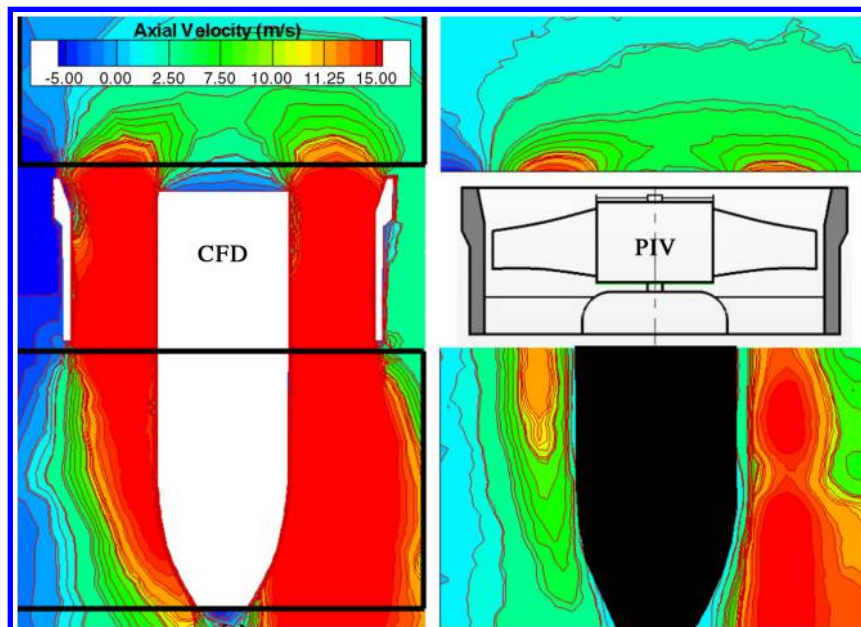


Fig. 21 Comparison of CFD and PIV axial velocity contours at an edgewise flight of 9000 rpm and 6 m/s.



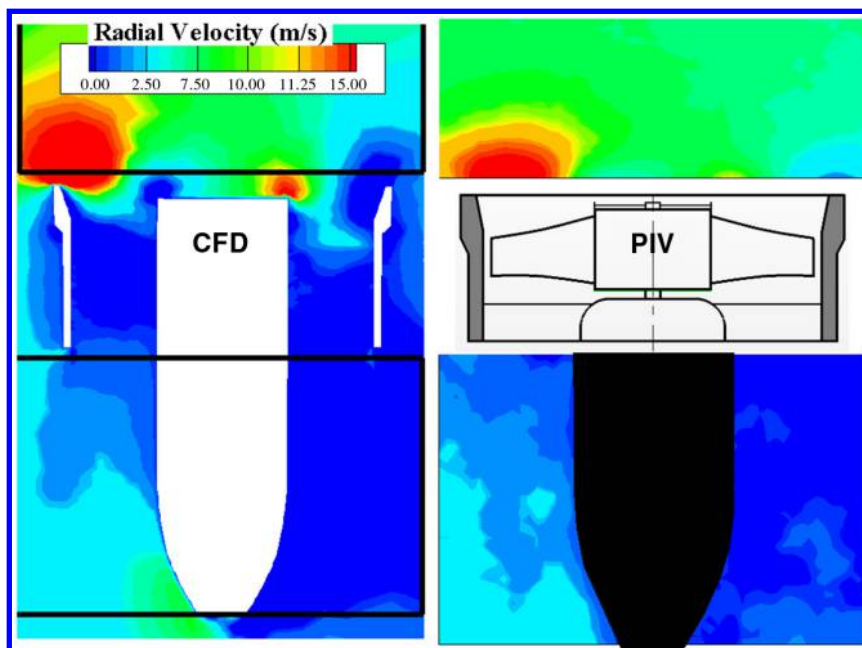


Fig. 22 Comparison of CFD and PIV velocity magnitude contours and streamlines at an edgewise flight of 9000 rpm and 6 m/s.

strong recirculatory flow characteristics. The current actuator disk approach neglects the hub separation features of the 5-in.-diam ducted fan.

## 2. Edgewise Flight Condition Results

The comparison of PIV measurements and computed axial and radial velocity components are shown in Figs. 21–23 for 6 m/s edgewise flight. The axial velocity computed at the inlet of the ducted fan shows good agreement with the PIV measurements. The computed radial velocity and velocity magnitude are also showing good agreement with PIV result. Flow near the hub is underpredicted because the rotating-hub-related viscous flow effects are not included in the current computations. It is also noted that the exit axial velocities are overpredicted. At the windward side of the ducted-fan, axial velocities are disturbed at the exit windward side of the ducted fan. Momentum deficits are shown to be higher in the PIV results near the tail cone at the leeward side of the ducted fan.

## VII. Conclusions

The velocity field around the ducted fan was measured using a planar PIV system. Axial and radial velocity components at the inlet/exit region of the ducted fan were measured in hover and edgewise flight at 6 m/s.

Besides the experimental study, a computational study based on solving incompressible Navier–Stokes equations was carried out. The specific radial equilibrium-based actuator disk fan model developed in this study uses a prescribed static pressure rise across the rotor disk for a time-efficient simulation of the fan rotor.

The results of the PIV measurements have proven that the performance of the ducted fan was highly affected from the crosswind velocity. In crosswind, by the effect of the edgewise flight velocity, a separation region restricting the effective breathing area of the fan rotor was always observed at the leading side of the ducted fan. That separation bubble significantly affected the exit flow of the fan rotor.

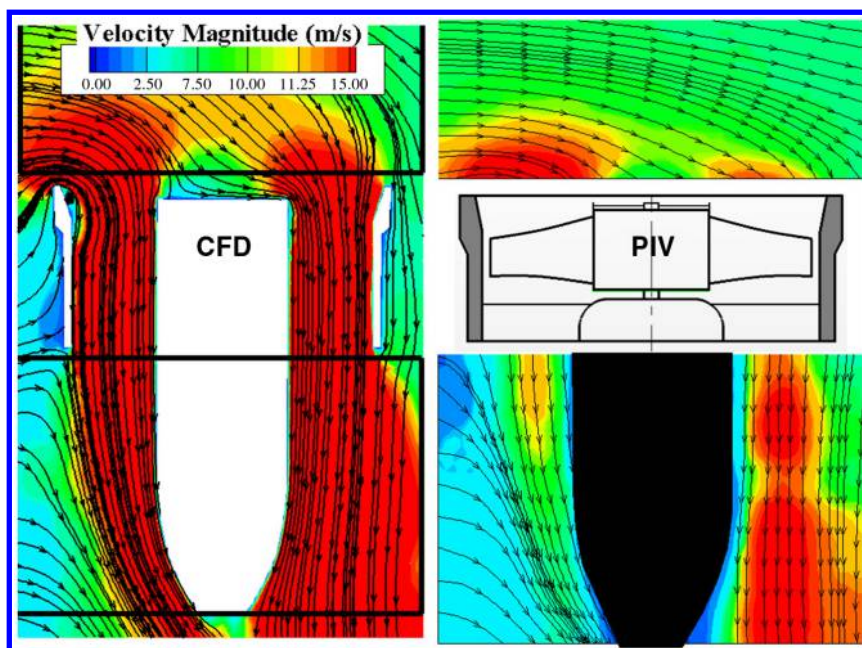


Fig. 23 Comparison of CFD and PIV velocity magnitude contours and streamlines at an edgewise flight of 9000 rpm and 6 m/s.

By the introduction of inlet distortion at the leading side, the flow characteristics of the fan were highly altered compared with the fan design conditions. The inlet flow distortion due to the leading-side lip separation resulted in a measurable drop in thrust force generated by the system.

The measured differentials existing between the leading side and trailing side of inlet flow are likely to generate excessive moment imbalance during the edgewise flight of the ducted-fan-based V/STOL UAV. The measured local flow differentials at the inlet plane directly translate into nonuniformities in the exit jet of the ducted fan.

The experimental results showed that an increase in the rotational speed of the fan enhances the axial velocity component at the inlet and exit sections in the hover condition, as expected. That increase in the rotational speed of the fan rotor improved the performance of the ducted fan in edgewise flight due to an improved axial momentum change in the ducted fan.

An increase in the rotational speed of the fan from 9000 to 15,000 rpm reduced the effect of the leading-side separation bubble.

The radial equilibrium-based simplified rotor model incorporated into a 3-D RANS-based computational analysis was able to predict the inlet flow axial flow velocity distribution well at the 9000 rpm hover condition. A comparison of the current PIV measurements and the accelerated RANS predictions supported by the simple radial equilibrium-based rotor model indicates that the current inviscid rotor model can be highly effective and time efficient in the design and optimization of future V/STOL UAV systems based on ducted-fan designs.

## References

- [1] Abrego, A. I., and Bulaga, R. W., "Performance Study of a Ducted Fan System," *AHS Aerodynamics, Aeroacoustic, Test and Evaluation Technical Specialist Meeting*, American Helicopter Soc., Alexandria, VA, 2002.
- [2] Martin, P., and Tung, C., "Performance and Flowfield Measurements on a 10-inch Ducted Rotor VTOL UAV," *60th Annual Forum of the American Helicopter Society*, American Helicopter Soc., Alexandria, VA, 2004.
- [3] Fleming, J., Jones, T., Lusardi, J., Gelhausen, P., and Enns, D., "Improved Control of Ducted Fan VTOL UAVs in Crosswind Turbulence," *AHS 4th Decennial Specialist's Conference on Aeromechanics*, 2004.
- [4] Lind, R., Nathman, J. K., and Gilchrist, I., "Ducted Rotor Performance Calculations and Comparisons with Experimental Data," 44th AIAA Aerospace Sciences Meeting and Exhibit, AIAA Paper 2006-1069, 2006.
- [5] Graf, W., Fleming, J., and Wing, N., "Improving Ducted Fan UAV Aerodynamics in Forward Flight," 46th AIAA Aerospace Sciences Meeting and Exhibit, AIAA Paper 2008-0430, 2008.
- [6] He, C., and Xin, H., "An Unsteady Ducted Fan Model for Rotorcraft Flight Simulation," *62nd AHS Forum*, American Helicopter Soc., Alexandria, VA, 2006.
- [7] Chang, I. C., and Rajagopalan, R. G., "CFD Analysis for Ducted Fans with Validation," 21st AIAA Applied Aerodynamics Conference, AIAA Paper 2003-4079, 2003.
- [8] Ahn, J., and Lee, K. T., "Performance Prediction and Design of a Ducted Fan System," 40th AIAA/ASME/SAE/ASEE Joint Propulsion Conference and Exhibit, AIAA Paper 2004-4196, 2004.
- [9] Ko, A., Ohanian, O. J., and Gelhausen, P., "Ducted Fan UAV Modeling and Simulation in Preliminary Design," AIAA Modeling and Simulation Technologies Conference and Exhibit, AIAA Paper 2007-6375, 2007.
- [10] Zhao, H. W., and Bil, C., "Aerodynamic Design and Analysis of a VTOL Ducted-Fan UAV," 26th AIAA Applied Aerodynamics Conference, AIAA Paper 2008-7516, 2008.
- [11] Adrian, R., "Particle Imaging Techniques for Experimental Fluid Mechanics," *Annual Review Of Fluid Mechanics*, Vol. 23, 1991, pp. 261–304.
- [12] Kahveci, H. S., and Camci, C., "Flow Around Helicopter Blade Tip Sections Using 2D Particle Image Velocimeter, Part 1," 11th International Symposium on Transport Phenomena and Dynamics of Rotating Machinery (ISROMAC-11) Paper 136, 2006.
- [13] Kahveci, H. S., and Camci, C., "Flow Around Helicopter Blade Tip Sections Using A (3-D) Stereoscopic Particle Image Velocimeter, Part 2," 11th International Symposium on Transport Phenomena and Dynamics of Rotating Machinery (ISROMAC-11) Paper 137, 2006.
- [14] Kahveci, H. S., *Implementation of a Stereoscopic PIV in Rotating Machinery Including Helicopter Rotor Flows*, M.S. Thesis, Pennsylvania State Univ., University Park, PA, 2004.
- [15] *FlowMap Particle Image Velocimetry Instrumentation: Installation and User's Guide*, DANTEC, Skovlunde Denmark, 2000.
- [16] Akturk, A., and Camci, C., "Axial Flow Fan Tip Leakage Flow Control Using Tip Platform Extensions," *Journal of Fluids Engineering*, Vol. 132, No. 5, 2010, Paper 051109. doi:10.1115/1.4001540